NRC Publications Archive
Archives des publications du CNRC

Magneli phase Ti4O7 electrode for oxygen reduction reaction and its implication for zinc-air rechargeable batteries

Li, Xiaoxia; Zhu, Aaron Li; Qu, Wei; Wang, Haijiang; Hui, Rob; Zhang, Lei; Zhang, Jiujun

This publication could be one of several versions: author's original, accepted manuscript or the publisher's version. / La version de cette publication peut être l'une des suivantes : la version prépublication de l'auteur, la version acceptée du manuscrit ou la version de l'éditeur.

For the publisher's version, please access the DOI link below./ Pour consulter la version de l'éditeur, utilisez le lien DOI ci-dessous.

NRC Publications Record / Notice d'Archives des publications de CNRC:
https://nrc-publications.canada.ca/eng/view/object/?id=a3bb453c-17dd-40b5-8380-706bc8708d6c
https://publications-cnrc.canada.ca/fra/voir/objet/?id=a3bb453c-17dd-40b5-8380-706bc8708d6c

Questions? Contact the NRC Publications Archive team at
PublicationsArchive-ArchivesPublications@nrc-cnrc.gc.ca. If you wish to email the authors directly, please see the first page of the publication for their contact information.

Vous avez des questions? Nous pouvons vous aider. Pour communiquer directement avec un auteur, consultez la première page de la revue dans laquelle son article a été publié afin de trouver ses coordonnées. Si vous n'arrivez pas à les repérer, communiquez avec nous à PublicationsArchive-ArchivesPublications@nrc-cnrc.gc.ca.

National Research Council Canada   Conseil national de recherches Canada

Canada

Magneli phase Ti_4O_7 electrode for oxygen reduction reaction and its implication for zinc-air rechargeable batteries

Xiaoxia Li, Aaron Li Zhu, Wei Qu*, Haijiang Wang, Rob Hui, Lei Zhang, Jiujun Zhang

Institute for Fuel Cell Innovation, National Research Council of Canada, 4250 Wesbrook Mall, Vancouver, BC V6P 1W5, Canada

ARTICLE INFO

ABSTRACT

In this paper, Magneli phase Ti_4O_7 was successfully synthesized using a TiO_2 reduction method, and characterized using X-ray diffraction, Raman spectroscopy, and X-ray photoelectron spectroscopy (XPS). The electrode coated with this Ti_4O_7 material showed activities for both the oxygen reduction reaction (ORR) and the oxygen evolution reaction (OER). For the ORR, several parameters, including overall electron transfer number, kinetic constants, electron transfer coefficient, and percentage H_2O_2 production, were obtained using the rotating ring-disk electrode (RRDE) technique and the Koutecky–Levich theory. The overall electron transfer number was found to be between 2.3 and 2.9 in 1, 4, and 6 M KOH electrolytes, suggesting that the ORR process on the Ti_4O_7 electrode was a mixed process of 2- and 4-electron transfer pathways. Electrochemical durability tests, carried out in highly concentrated KOH electrolyte, confirmed that this Ti_4O_7 is a stable electrode material, suggesting that it should be a feasible candidate for the air-cathodes of zinc-air batteries. To understand the stability of this material, Raman and XPS spectra were also collected for the Ti_4O_7 samples before and after the stability tests. The results and analysis revealed that a thin layer of TiO_2 formed on the Ti_4O_7 surface, which may have prevented further oxidation into the bulk of the Ti_4O_7 electrode.

1. Introduction

Zinc-air rechargeable batteries (ZARBs) have drawn great attention in recent years due to their high specific energy, low cost, and safety. It has been recognized that ZARBs could be used in several important power-intensive areas, such as portable and back-up power, and automobile applications. However, several major challenges still exist at the current stage of technology, including relatively low performance and insufficient stability in the bi-functional air-cathode [1–3].

The major reason for the low stability of air-electrodes in ZARBs is carbon material corrosion or oxidation in the presence of oxygen and at high electrode potentials. The air-cathode reaction layer for both electrochemical reactions and for gas diffusion is a matrix structure containing primarily carbon particles and ionomer. During the electrochemical reactions inside this layer, these carbon particles serve as the reaction sites for the oxygen reduction reaction (ORR) and the oxygen evolution reaction (OER) during battery discharging and charging, respectively. For a zinc-air rechargeable battery, the electrolyte is a concentrated alkaline solution. Under these conditions, the kinetically slow but thermodynamically favoured carbon oxidation into carbonate during battery operation can proceed [4]. Ross and Sokol [5] studied this corrosion process in alkaline solutions using ^{14}C labelling technique, and found that oxidative carbon dissolution and gasification (to carbon monoxide) occurred at different temperatures and applied potentials. Impedance analysis of rechargeable metal-air batteries also showed that electrode deterioration during anodic oxygen evolution was mainly due to carbon corrosion, resulting in a loss in electrochemical active surface area [1]. In addition, the ORR on carbon material in alkaline electrolyte is mainly a 2-electron transfer process forming hydrogen peroxide [6], which is a strong oxidizer, attacking electrode materials such as carbon and deteriorating the overall stability of the air-cathode [7]. Therefore, corrosion of carbon by oxidation can reduce the reaction site density, leading to battery performance degradation.

As mentioned above, carbon materials do not seem stable enough for air-cathodes in zinc-air rechargeable batteries due to carbon corrosion in the presence of O_2 and H_2O_2 (an ORR product), and at high electrode potentials. Therefore, developing more stable non-carbon support materials for air-cathodes seems necessary. In recent years, conductive Magneli phase materials such as Ti_nO_{2n-1} ($4 < n < 10$) have been explored as electrode materials or conductive supports in electrochemical systems, including fuel cells, because of their high conductivities and relatively high corrosion-resistivity in aggressively acidic and alkaline electrolytes

[4,8,9]. Among this series of distinct mixed-valence oxides, Ti_4O_7 exhibits the highest electrical conductivity, exceeding $1000\,S\,cm^{-1}$ at room temperature, which is even higher than the $727\,S\,cm^{-1}$ of graphitized carbon [10,11]. This superior conductivity, combined with its electrochemical stability, has made Ti_4O_7 a promising air-cathode candidate. In addition, because titanium is also one of the most abundant elements on earth, Ti_4O_7 would be a cost-effective battery material.

To explore Ti_4O_7 as an air-cathode material for zinc-air rechargeable batteries, in particular under strong alkaline conditions, we synthesized and characterized this material. Ti_4O_7 powder was synthesized by reducing anatase TiO_2 through a controlled reduction process. The crystalline phase and morphology of Ti_4O_7 powder were examined by X-ray diffraction (XRD), micro-Raman spectroscopy, and high-resolution scanning electron microscopy (HRSEM). The electrochemical properties of Ti_4O_7 were also studied using cyclic voltammetry (CV), rotating disk electrode (RDE), and rotating ring-disk electrode (RRDE) techniques in electrolyte solutions containing various concentrations of KOH. The electrochemical stability of the as-prepared Ti_4O_7 powder was also evaluated by cyclic voltammetry scans and chronopotentiometric tests. We concluded that this material is potentially usable in air-cathodes for zinc-air rechargeable batteries.

2. Experimental

2.1. Ti_4O_7 synthesis

Ti_4O_7 powder was synthesized by reducing anatase TiO_2 powder (Alfa-Aesar, 99.9%, 32 nm particles, surface area $45\,m^2\,g^{-1}$) at $950\,°C$ with pure H_2 flow (Proxair, 99.99%) at a rate of $200\,mL\,min^{-1}$ for 4 h. In addition, a Ti_4O_7 pellet was made by reducing a TiO_2 pellet at $1150\,°C$ for 2 h; the TiO_2 pellet had been created in-house using TiO_2 powder shaped under 70 MPa pressure for 3 min in a 5 mm diameter circular die, then sintered at $1350\,°C$ for 4 h in air. The Ti_4O_7 pellet was used to simulate air-cathode conditions in zinc-air rechargeable batteries, in order to test its electrode stability in 6 M KOH solution saturated with O_2. Both powder and pellet appeared dark blue after H_2 reduction, suggesting the Ti_4O_7 material had a characteristic of oxygen deficient crystal structure.

2.2. Ti_4O_7 structure characterization

The morphologies of samples were examined using a field emission scanning electron microscope (FESEM, Hitachi S-4700). The specific surface area measurements were carried out via the gas adsorption technique (BET) on a surface area analyzer (Beckman Coulter, SA3100). The samples' chemical states were examined by X-ray photoelectron spectroscopy (XPS) using a Leybold MAX200 system (Leybold, Germany) operated with a Mg Kα source (1253.6 eV) at 10 kV and 20 mA, with a 48 eV pass energy and the analytical chamber at 2×10^{-9} mbar; all reported binding energies were referenced to the adventitious hydrocarbon C 1s peak at 285.0 eV. The laser-induced effect on Ti_4O_7 was monitored by Micro-Raman equipped with an XploRA Spectrometer (HORIBA Jobin Yvon). The Raman spectra were acquired with a 532 nm laser source (laser power with no attenuation: 15.4 mW) and $100\times$ objective (detective spot size: 1 μm). The laser energy filter was set to 10%, 20%, 50%, and 100%. The crystal phase of Ti_4O_7 was assessed by X-ray diffraction (XRD), and the XRD data were collected with a Bruker D8 Advance diffractometer (Bruker, Cu K α1 source, $\lambda = 1.5406\,Å$) over the range $10–90°$ $2\theta–2\theta$ at a scanning rate of $0.01°\,s^{-1}$.

2.3. Working electrode preparation

A glassy carbon disk electrode, geometric area $0.16\,cm^2$, was used as the substrate electrode on which a thin layer containing Ti_4O_7 and Nafion ionomer was coated to form the working electrode. In the electrode coating process, an ultrasonically dispersed 20 μL ink containing 100–120 μg of Ti_4O_7 in appropriate 2-propanol aqueous solution was carefully cast onto the top of the glassy carbon disk using a micropipette; the disk was in the middle of a rotating ring (Pt)-disk (glassy carbon) electrode (RRDE). Next, 3.9 μL of 0.5 wt% Nafion aqueous solution (diluted from 5 wt% Nafion solution, DuPont) was pipetted onto the Ti_4O_7 layer, and the electrode was left to dry in air under a 20 W lamp.

2.4. Electrochemical measurements

Electrochemical measurements for the Ti_4O_7 coated electrode were conducted using a Solartron Analytical 1470E Cell Test System. A conventional electrochemical cell containing three electrodes was used for all cyclic voltammetry, rotation ring-disk electrode, and potential holding measurements. For the RRDE working electrode (AFE7R9GCPT, Pine Research Inc.), the glassy carbon disk and platinum ring had geometric areas of 0.16 and $0.036\,cm^2$, respectively. The ring electrode collection efficiency of this RRDE was measured using a 10 mM $K_3[Fe(CN)_6]$ solution (Fischer Scientific, 98+%) in nitrogen-saturated 0.1 M KOH, and found to be 0.20. The counter electrode was a Pt mesh and the reference electrode was a commercially available Hg/HgO electrode (CH Instruments, Inc.). Deionized water (Millipore SuperQ system, resistivity 18 MΩ cm) was used to prepare electrolyte solutions with various concentrations of KOH. For surface cyclic voltammetry measurements, the solution was bubbled before each measurement with pure N_2 (99.9%) for 30 min to remove dissolved O_2, and for ORR measurements, the solution was bubbled with pure O_2 (99.9%) for 30 min.

For electrochemical stability tests of the Ti_4O_7 powder, cyclic voltammetry scanning between −0.7 and +0.7 V vs. Hg/HgO at a potential scan rate of $0.05\,V\,s^{-1}$ was performed for 5000 cycles in O_2-saturated 6 M KOH solution. In order to simulate air-cathode conditions in a zinc-air rechargeable battery, the Ti_4O_7 pellet electrode was also tested by holding the electrode potential at 0.55 V vs. Hg/HgO for 360 h in O_2-saturated 6 M KOH solution.

3. Results and discussion

3.1. Structural and morphological characterization

To confirm the identity of the synthesized material, high-resolution XRD patterns were collected using the as-prepared Ti_4O_7 powder. The results are presented in Fig. 1, which shows that the XRD patterns, including the fingerprint peaks and their relative intensities, are almost identical to standard values (JCPDS-ICDD File No. 01-071-1428), indicating that the synthesized sample was a pure triclinic phase of Ti_4O_7.

To examine the morphology of the synthesized Ti_4O_7 powder, high-resolution SEM (HRSEM) images were collected, as shown in Fig. 2(a) and (b). The material had a macroporous structure with an average particle size of ca. 0.5–1 μm. BET measurement was also conducted on this material, and gave a surface area of $2.7\,m^2\,g^{-1}$. A macroporous structure such as this is believed to be desirable for gas transfer within a matrix, in particular when the material is used to construct battery air-cathodes.
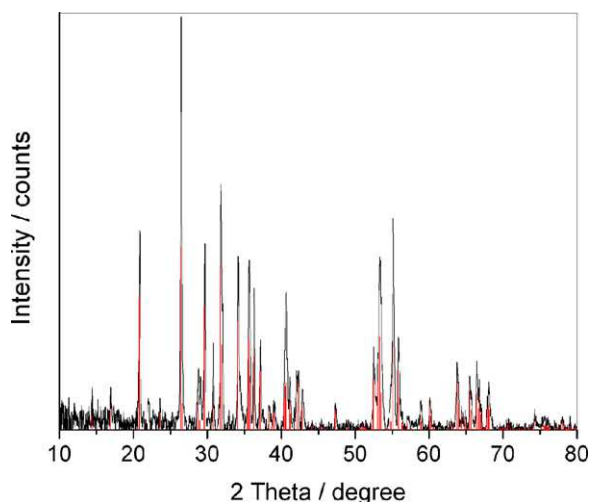
Fig. 1. Typical XRD pattern of the as-prepared Ti_4O_7 powder. Vertical lines are for standard XRD peak positions of pure Ti_4O_7.

3.2. Electrochemical characterization—ORR kinetic constants on Ti_4O_7 electrode in concentrated KOH solutions

To test the ORR activity of the synthesized material, the electrode coated with Ti_4O_7 was put into an O_2-saturated 6 M KOH solution to obtain cyclic voltammetry (CV) measurements for the ORR and OER. The results are shown in Fig. 3, and indicate that the Ti_4O_7 was active for both reactions. The downward peak at ca. −0.19 V vs. Hg/HgO with an onset potential of −0.12 V comes from
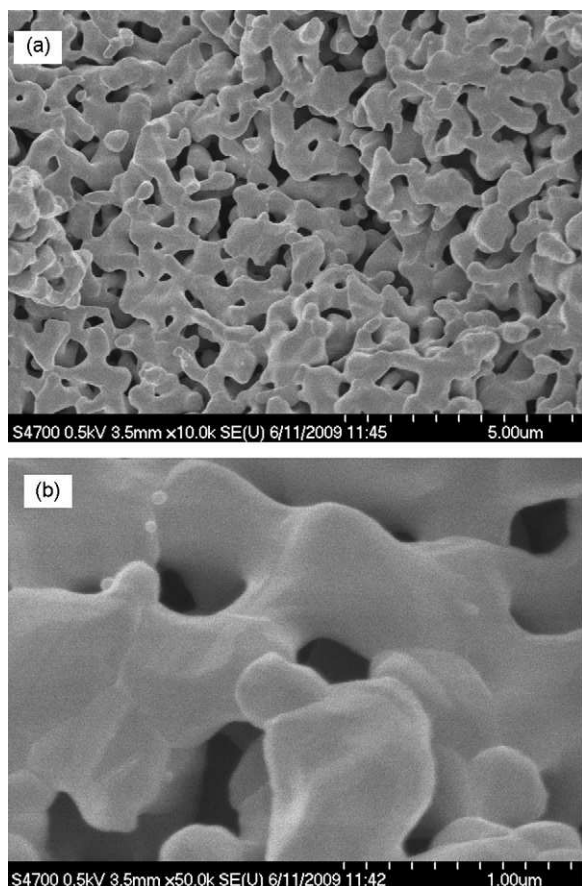

Fig. 2. Typical HRSEM images of the as-prepared Ti_4O_7 powder. *Note*: (a) and (b) have different scales.
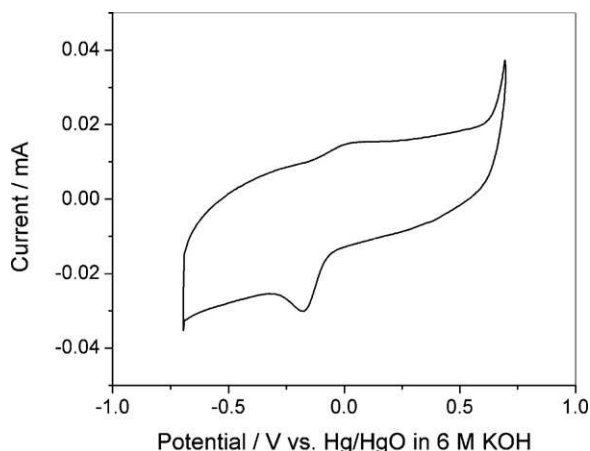

Fig. 3. 50th curve of steady-state cyclic voltammogram for Ti_4O_7 coated electrode in O_2-saturated 6 M KOH solution at room temperature. Ti_4O_7 loading: ca. 1.4 mg cm^{-2}. Potential scan rate: 50 mV s^{-1}.

the ORR, and the upward current with an onset potential of 0.64 V arises from the OER. These electrode activities for the ORR and OER suggest that the Ti_4O_7 material synthesized in this study should be a good candidate for air-cathodes in zinc-air rechargeable batteries.

For more quantitative evaluation of the ORR activity on the Ti_4O_7 electrode, RRDE technique was employed to obtain the kinetic information in 1, 4, and 6 M KOH solutions. Fig. 4 shows the typical RRDE disk and ring currents in 6 M KOH, collected at rotation rates from 400 to 2500 rpm. The ORR on the Ti_4O_7 electrode was under kinetic control in the potential range of ca. −0.05 to −0.15 V, under combined kinetic-diffusion control from ca. −0.15 to −0.20 V, and reached the limiting current at higher overpotentials (>−0.20 V). Based on the current–voltage data shown in Fig. 4, several ORR kinetic parameters can be obtained, as follows.

To obtain a greater understanding of the ORR on this Ti_4O_7 electrode, the overall electron transfer number (n) and the corresponding mole percentage of H_2O_2 (mol% H_2O_2) produced in the ORR process were calculated via RRDE theory. According to this theory, n and mol% H_2O_2 can be determined using Eqs. (1) and (2), respectively [12,13]:

$$n = \frac{4i_d}{i_d + (i_r/N)} \quad (1)$$
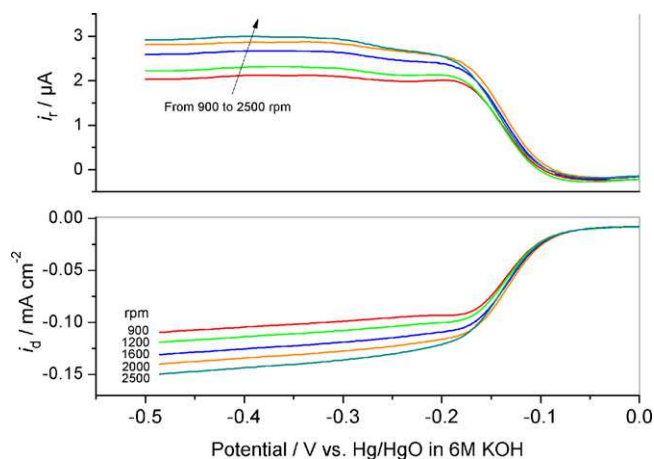
Fig. 4. Rotating ring-disk current–voltage curves at different electrode rotation rates as marked in the figure. Disk currents were recorded on Ti_4O_7 coated glassy carbon disk electrode in potential range 0.0 to −0.50 V vs. Hg/HgO, and ring currents were recorded on platinum ring electrode with fixed potential of +0.5 V in O_2-saturated 6 M KOH solution. Potential scan rate: 5 mV s^{-1}. Ti_4O_7 loading on disk electrode: 0.73 mg cm^{-2}.
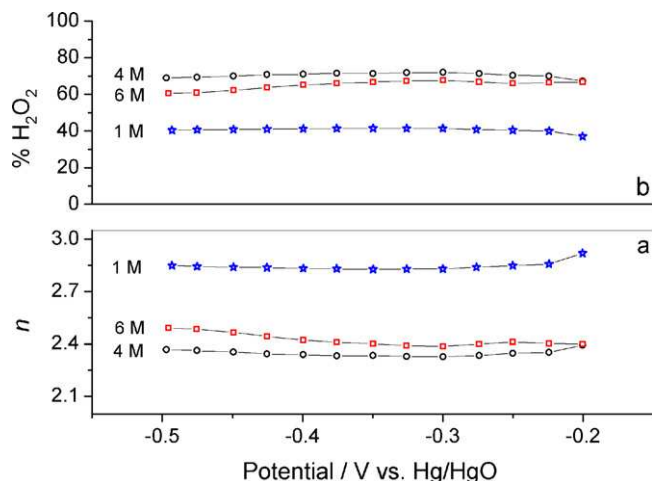
Fig. 5. (a) Plots of overall electron transfer number and (b) percentage H_2O_2 produced as a function of electrode potential at three different concentrations of O_2-saturated KOH solution. Calculations based on data in Fig. 4. Electrode rotation rate: 1600 rpm.

$$\%H_2O_2 = 100 \cdot \frac{i_r/i_d}{N} \tag{2}$$

Here, i_d is the current on the disk electrode, i_r is the current on the ring electrode, and N is the collection coefficient of the ring electrode (=0.20). Based on Fig. 4 and Eqs. (1) and (2), the overall electron transfer numbers and corresponding percentage of H_2O_2 produced in the ORR process on the Ti_4O_7 electrode in 1, 4, and 6 M KOH were calculated, and are summarized in Fig. 5(a) and (b). The overall electron transfer numbers in these KOH solutions are in the range of 2.3–2.9, with the corresponding percentages of H_2O_2 being 35–72%. These results suggest that the ORR on Ti_4O_7 is a mixed process of 2- and 4-electron transfer pathways. However, the higher the KOH concentration, the greater the amount of H_2O_2 detected (or the lower the overall electron transfer number). It is understandable that in a more concentrated alkaline medium, H_2O_2 in the form of HO_2^- will be more stable than in a less concentrated OH^- solution.

The ORR mechanism was further explored using the Koutecky–Levich theory (i.e., rotating disk electrode theory [14]). According to this theory, the current at the disk electrode (i_d, A) can be expressed as Eq. (3):

$$\frac{1}{i_d} = \frac{1}{i_k} + \frac{1}{i_{dl}} \tag{3}$$

where i_k and i_{dl} are the kinetic and diffusion-limiting currents, respectively. Furthermore, i_k and i_{dl} (both in an unit of A) can be expressed as Eqs. (4) and (5), respectively:

$$i_k = nFAkC_{O_2} \tag{4}$$

$$i_{dl} = 0.20nFAC_{O_2}D_{O_2}^{2/3}\nu^{-1/6}\omega^{1/2} = Bn\omega^{1/2} \tag{5}$$

where n is the overall electron transfer number in the ORR, F is the Faraday constant (96,500 C mol^{-1}), A is the geometric area of the
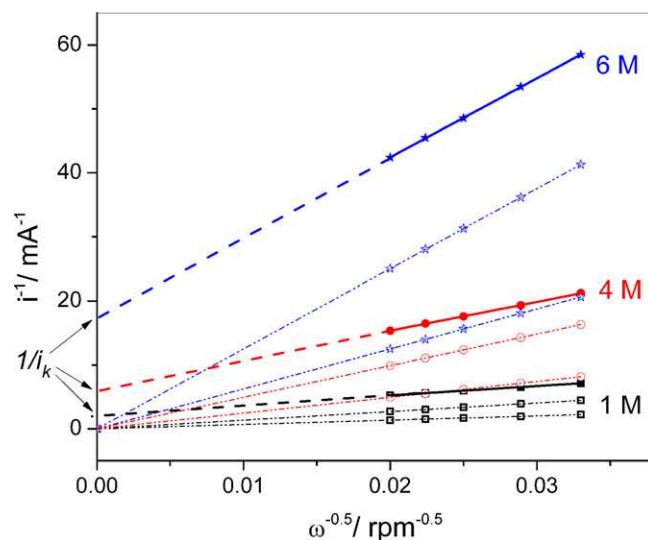

Fig. 6. Koutecky–Levich plots for ORR on Ti_4O_7 electrode at −0.40 V vs. Hg/HgO in 1 M (solid black line), 4 M (solid red line), and 6 M KOH (solid blue line) solutions; theoretical plots for 2- and 4-electron transfer process are also displayed as dashed lines, for comparison. (For interpretation of the references to color in this figure caption, the reader is referred to the web version of the article.)

disk electrode (0.16 cm^2), C_{O_2} (mol cm^{-3}) is the concentration of oxygen dissolved in the electrolyte solution, D_{O_2} (cm^2 s^{-1}) is the diffusion coefficient of oxygen, ν (cm^2 s^{-1}) is the kinematic viscosity of the electrolyte, ω (rpm) is the electrode rotation rate, and k (cm s^{-1}) is the rate constant for the ORR. In concentrated alkaline solutions, the solubility and diffusion coefficient of oxygen as well as the kinematic viscosity of the electrolyte are strongly dependent on the KOH concentration [15]. The corresponding parameters in 1, 4, and 6 M KOH are listed in Table 1. From these parameters [16,17], the value of B in Eq. (5) and the theoretical slopes ($1/Bn$) for $n = 2$ and $n = 4$ in the Koutecky–Levich plots (K–L plots) were determined and are summarized in Table 1.

Fig. 6 shows the Koutecky–Levich plots for the ORR on Ti_4O_7 electrode in 1, 4, and 6 M KOH. The theoretical plots for the 2- and 4-electron transfer processes towards the ORR are also displayed for comparison. All plots clearly show a linear and parallel feature at a series of potentials in 1, 4, and 6 M KOH, suggesting a first-order kinetics with respect to oxygen concentration [18]. All slopes of the Koutecky–Levich plots are located between the theoretical 2- and 4-electron transfer lines, suggesting that the ORR process catalyzed by Ti_4O_7 is a mixture of 2- and 4-electron transfer pathways; this conclusion is consistent with the conclusion drawn from Fig. 5. Koutecky–Levich plots were also obtained at different electrode potentials, from −0.12 to −0.40 V, for three KOH concentrations (not shown here), based on which the kinetic currents (i_k) of the ORR were calculated from the intercept of the Koutecky–Levich plots at $\omega^{-1/2} = 0$. Based on the i_k values, the corresponding values for the ORR kinetic rate constant (k) under various conditions are listed in Table 2.

Table 1
Solubilities of oxygen (C_{O_2}, mol cm^{-3}), the diffusion coefficients of oxygen (D_{O_2}, cm^2 s^{-1}), the kinematic viscosities of the electrolyte (ν, cm^2 s^{-1}), the values of the calculated B, and the theoretical slopes for $n = 2$ and $n = 4$ in line of $i_d^{-1} - \omega^{-1/2}$ in 1, 4, and 6 M KOH, respectively.

Electrolyte solutions	[a] C_{O_2} (mol cm^{-3})	[a] D_{O_2} (cm^2 s^{-1})	[b] ν (cm^2 s^{-1})	B (mA rpm$^{-1/2}$)	Slope (mA^{-1} rpm$^{1/2}$) $n = 2$	Slope (mA^{-1} rpm$^{1/2}$) $n = 4$
1 M	0.83×10^{-6}	1.65×10^{-5}	0.95×10^{-2}	3.58×10^{-3}	136	68
4 M	0.33×10^{-6}	1.05×10^{-5}	1.23×10^{-2}	1.02×10^{-3}	495	247
6 M	0.17×10^{-6}	0.78×10^{-5}	1.52×10^{-2}	0.41×10^{-3}	1250	625

[a] The values are from Ref. [16].
[b] The values are from Ref. [17].

Table 2
Comparison of the Koutechy–Levich data of Ti_4O_7 electrode at various potentials in 1, 4 and 6 M KOH solutions.

Electrode potential (E)	1 M			4 M			6 M		
	Intercept (mA^{-1})	i_k (mA)	k ($cm\,s^{-1}$)	Intercept (mA^{-1})	i_k (mA)	k ($cm\,s^{-1}$)	Intercept (mA^{-1})	i_k (mA)	k ($cm\,s^{-1}$)
−0.12	243	0.0041	1.6×10^{-4}	195	0.0051	4.0×10^{-4}	110	0.0091	1.7×10^{-3}
−0.14	121	0.0083	3.2×10^{-4}	106	0.0094	7.4×10^{-4}	66	0.015	2.8×10^{-3}
−0.16	58	0.017	6.5×10^{-4}	59	0.017	1.3×10^{-3}	47	0.021	3.9×10^{-3}
−0.18	29	0.034	1.3×10^{-3}	36	0.028	2.2×10^{-3}	37	0.027	5.0×10^{-3}
−0.20	16	0.063	2.4×10^{-3}	24	0.042	3.2×10^{-3}	30	0.033	6.1×10^{-3}
−0.25	5.7	0.18	6.7×10^{-3}	13	0.077	6.3×10^{-3}	20	0.050	9.3×10^{-3}
−0.30	3.6	0.28	1.1×10^{-2}	9.3	0.11	8.5×10^{-3}	19	0.054	1.0×10^{-2}
−0.35	2.9	0.34	1.3×10^{-2}	8.0	0.13	1.0×10^{-2}	18	0.055	1.0×10^{-2}
−0.40	2.6	0.38	1.5×10^{-2}	7.2	0.14	1.1×10^{-2}	18	0.057	1.1×10^{-2}

It can be seen from Table 2 that the ORR rate constant (k) is strongly dependent on the electrode potential. Note that the i_k obtained at $\omega^{-1/2} = 0$ from Fig. 6 should contain two contributions: one from the chemical reaction (O_2 reacts with the active site on the electrode surface before electron transfer occurs), and the other from the electron transfer in the rate-determining step (RDS) for the overall ORR. Hence, this rate constant (k) may contain two contributions, and therefore the relationship between the kinetic constant (k) and the electrode potential may be expressed as Eq. (6):

$$\frac{1}{k} = \frac{1}{k_c} + \frac{1}{k_e \exp(-(\alpha n_\alpha F/RT)(E - E^o))} \tag{6}$$

where k_c is the chemical reaction rate constant between O_2 and the active reaction site on the electrode surface before electron transfer, k_e is the electron transfer rate constant in the rate-determining step of the overall ORR, α is the electron transfer coefficient in the RDS, n_α is the electron transfer number in the RDS (for the ORR process on an electrode, the electron transfer number in the rate-determining step is accepted as 1 [19]), E is the applied electrode potential, and E^o is the thermodynamic electrode potential under the measurement conditions. From Table 2 it can be seen that when electrode potential is below −0.30 V, the kinetic constant (k) is almost independent of the electrode potential, suggesting that the second term in Eq. (6) can be negligible and the overall kinetic constant should be equal to the chemical reaction rate constant, that is, $k = k_c$. Averaging the k values at −0.30, −0.35, and −0.40 V gives the chemical reaction constant. The obtained k_c values for 1, 4, and 6 M KOH are 1.3×10^{-2}, 9.8×10^{-3}, and 1.0×10^{-2} cm s^{-1}, respectively. These values are fairly close, ($\sim 1.0 \times 10^{-2}$ cm s^{-1}), indicating that the OH^- concentration has an insignificant effect on the chemical reaction between O_2 and Ti_4O_7. With this k_c value of 1.0×10^{-2} cm s^{-1}, Eq. (6) can be rearranged as Eqs. (7) and (8) for the ORR on Ti_4O_7 electrode in the KOH concentration range of 1–6 M:

$$\frac{1}{k} = 100 + \frac{1}{k_e} \exp(\frac{\alpha n_\alpha F}{RT}(E - E^o)) \tag{7}$$

$$\log\left(\frac{1}{k} - 100\right) = \log\left(\frac{1}{k_e}\right) + 2.303 \frac{\alpha n_\alpha F}{RT}(E - E^o) \tag{8}$$

In Eq. (8), E^o can be obtained using a Nernst Equation (9) for the ORR ($O_2 + 2H_2O + 4e^- \leftrightarrow 4OH^-$):

$$E^o = E^{o'} + \frac{2.303RT}{nF} \log\left(\frac{[O_2]}{[OH^-]^4}\right) \tag{9}$$

where $E^{o'}$ is the standard electrode potential of the ORR at 25 °C, 1 atm pressure of O_2, and 1 M of OH^-, which is 0.401 V (vs. NHE); $[O_2]$ is the dissolved O_2 molar concentration under 1 atm pressure; $[OH^-]$ is the solution's molar OH^- concentration; and R, T, n, and F are the same as defined in Eqs. (5) and (6). According to Eq. (9) and the data in Table 1, the calculated values for E^o at the three different KOH concentrations are 0.375, 0.305, and 0.276 V (vs. NHE), respectively.
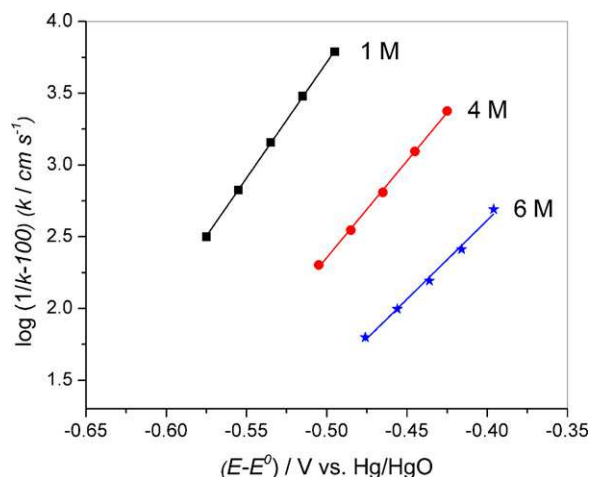
Fig. 7. ORR kinetic constants as a function of applied electrode potential ($E - E^o$) at three different KOH concentrations, based on data in Table 2.

According to Eq. (8) and based on the data in Tables 1 and 2, the plots of $\log(1/k-100)$ vs. ($E - E^o$) can be obtained in the potential range of −0.12 to −0.20 V, as shown in Fig. 7, where the plots all display a linear relationship. From the intercepts of these linear plots at $E = E^o$, k_e values at the three different KOH concentrations can be obtained, and from the slopes, the values of α can also be calculated if n_α is taken as 1 (Table 3).

Another important parameter is the exchange current density (i^o). If i^o can be defined by Eq. (10), its value at different KOH concentrations can be calculated based on the value of k_e:

$$i^o = nFC_{O_2}k_e \tag{10}$$

The values for i^o at three different KOH concentrations, based on Eq. (10), are listed in Table 3, together with the corresponding values of k_e and α. Obviously, different k_e, i^o, or α values reflect the effect of KOH concentration on the ORR kinetics on a Ti_4O_7 electrode. The exchange current densities and electron transfer rate constants greatly increased with rising alkaline concentration.

It is worthwhile to point out that the RDE theory expressed by Eq. (3) should be modified if a porous layer electrode rather than a smooth electrode is used. The effect arises from the thickness

Table 3
Electron transfer rate constant (k_e), and the electron transfer coefficiency (α) in the ORR rate-determining step, calculated based on the intercept and the slope values obtained in Fig. 7. The electron transfer number (n_α) in the ORR rate-determining step was taken as 1.
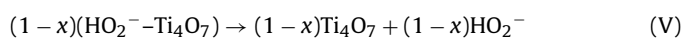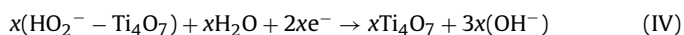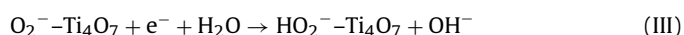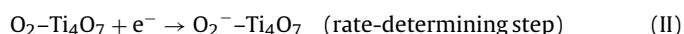
Electrolyte solutions	1 M	4 M	6 M
k_e ($cm\,s^{-1}$)	1.6×10^{-12}	8.1×10^{-10}	9.8×10^{-8}
i^o ($mA\,cm^{-2}$)	3.8×10^{-10}	7.7×10^{-8}	4.8×10^{-6}
α	0.19	0.15	0.12

of Nafion® ionmer porous layer which could limit the diffusion of O_2 within the electrode [20]. In this work, we did some calculations and found that the thickness effect of ionomer layer on the values of i_k is insignificant, and therefore can be ignored.

3.3. Discussion of the ORR mechanism

As described above, the ORR mechanism on a Ti_4O_7 electrode is a combination of 2- and 4-electron transfer pathways. The oxygen adsorbed on the electrode surface can be electrochemically reduced through several elementary steps. The H_2O_2 produced (in the form of HO_2^- in alkaline solution) after two electrons can then be further reduced to water or can dissolve into the solution, depending on the electrode material used. If the HO_2^- is relatively stable, it can enter into the solution before being further reduced by another two electrons to H_2O. This dissolved HO_2^- will be detected by the ring electrode when the RRDE is rotated.

Based on the literature [21–23] and our understanding, the ORR mechanism on the Ti_4O_7 surface may be proposed through several steps, as presented in Reactions (I)–(V):

$$Ti_4O_7 + O_2 \rightarrow O_2{-}Ti_4O_7 \qquad (I)$$

$$O_2{-}Ti_4O_7 + e^- \rightarrow O_2^-{-}Ti_4O_7 \quad \text{(rate-determining step)} \qquad (II)$$

$$O_2^-{-}Ti_4O_7 + e^- + H_2O \rightarrow HO_2^-{-}Ti_4O_7 + OH^- \qquad (III)$$

$$x(HO_2^- - Ti_4O_7) + xH_2O + 2xe^- \rightarrow xTi_4O_7 + 3x(OH^-) \qquad (IV)$$

$$(1-x)(HO_2^-{-}Ti_4O_7) \rightarrow (1-x)Ti_4O_7 + (1-x)HO_2^- \qquad (V)$$

In this mechanism, Reaction (I) is the chemical reaction discussed above. This reaction has a reaction rate constant of 1.0×10^{-2} cm s^{-1}, as determined by RDE measurements. Reaction (II) is the ORR rate-determining step on the electrode surface, whose rate constants are listed in Table 2. Reaction (III) represents the reactions for peroxide formation. After HO_2^- formation, HO_2^- can go in one of two ways: further 2-electron reduction to OH^- through Reaction (IV), or chemical desorption through Reaction (V) to form a free peroxide ion, which then enters into the bulk solution and can be detected by the ring electrode of the RRDE. As discussed above, the ORR on the Ti_4O_7 electrode has a mixed 2- and 4-electron transfer pathway, giving an overall electron transfer number of less than 4. The relative portion of Reaction (IV) can be expressed as x, and the portion of Reaction (V) can be expressed as $(1-x)$. When $x = 1$, the mechanism will follow a totally 4-electron transfer pathway, and when $x = 0$, the mechanism will be a totally 2-electron pathway. If the x value is larger than 0 and smaller than 1, the ORR will have a mixed 2- and 4-electron transfer pathway, as is the case in Fig. 4. Note that this ORR mechanism is only hypothetical, to facilitate understanding. More evidence is needed to validate the mechanism.

3.4. Stability tests and diagnosis for Ti_4O_7 electrode in O_2-saturated KOH solution

For any electrode material used in zinc-air rechargeable batteries, long-term stability is critical. In order to test the practical feasibility of the synthesized Ti_4O_7 material, the stability of the Ti_4O_7 electrode was tested in an O_2-saturated alkaline solution using cyclic voltammetry in the potential range of −0.70 to +0.70 V vs. Hg/HgO. As Fig. 8 shows, the Ti_4O_7 electrode survived 5000 cycles without significant loss in the ORR peak current (which was ca. −0.19 V), suggesting that Ti_4O_7 would be a stable material for air-cathodes in zinc-air rechargeable batteries. Inductively coupled plasma (ICP) analysis was carried out as well to track the concentration of dissolved Ti species in electrolytes, and the concentration of Ti^{4+} after the CV test was found to be below 0.1 mg L^{-1}, further demonstrating the stability of the Ti_4O_7 material.
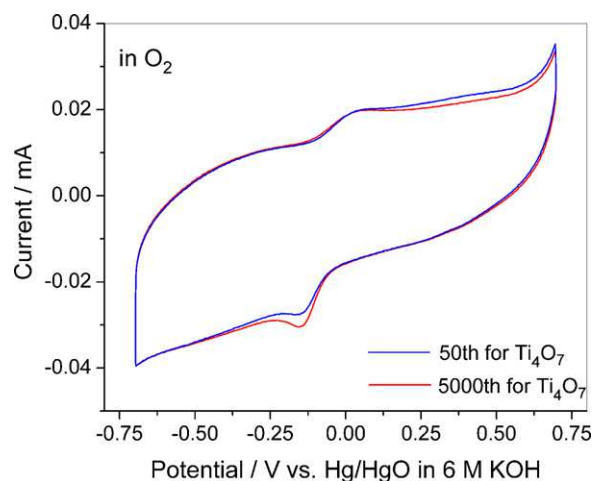

Fig. 8. Cyclic voltammograms of Ti_4O_7 electrode before (solid blue curve) and after (solid red curve) potential cycling between −0.7 V and +0.7 V for 5000 cycles in O_2-saturated 6 M KOH electrolyte. Potential scan rate: 50 mV s^{-1}. (For interpretation of the references to color in this figure caption, the reader is referred to the web version of the article.)

A high-potential holding test was also conducted on the Ti_4O_7 pellet for 360 h at a constant potential of 0.55 V vs. Hg/HgO in O_2-saturated 6 M KOH (Fig. 9). Initially, the current decreased gradually, then remained constant at ca. 66% of the original value for 360 h, indicating that this Ti_4O_7 was reasonably stable in 6 M KOH.

3.5. Surface characterization using Raman spectroscopy and XPS

To study the possible degradation mechanism of the Ti_4O_7 material, the material surfaces before and after long-term tests were examined using both Raman and XPS techniques. Normally, the crystal structure of Magneli compound Ti_4O_7 is built from successive blocks of rutile TiO_2, which were separated by two-dimensional shear planes to form Ti_4O_7 [24,25]. Fig. 10(a) displays the Raman spectra for the Ti_4O_7 samples before stability testing. With a 10% energy filter, only one broad band, at 140 cm^{-1}, can be observed (Fig. 10(a)-1). This spectrum is consistent with what is reported in the literature for the metallic high-temperature phase of Ti_4O_7 [24]. However, obvious changes occurred as the energy filter was set to 25% and beyond (not shown). Three additional bands at 255, 418, and 603 cm^{-1} can be seen in Fig. 10(a)-2, which corre-
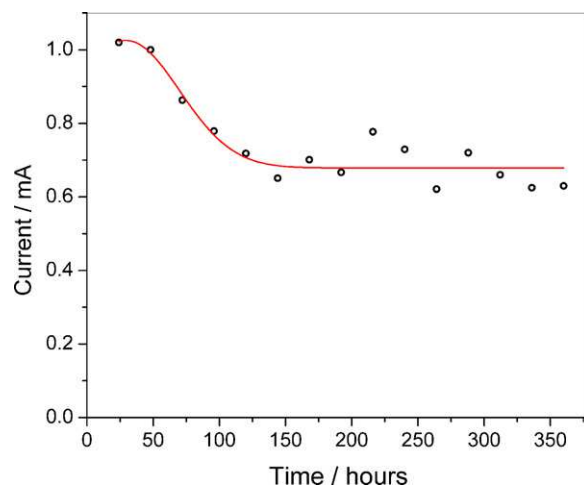

Fig. 9. Stability curve recorded during high-potential holding test using Ti_4O_7 pellet electrodes in O_2-saturated 6 M KOH electrolyte for 360 h; potential kept at 0.55 V vs. Hg/HgO.
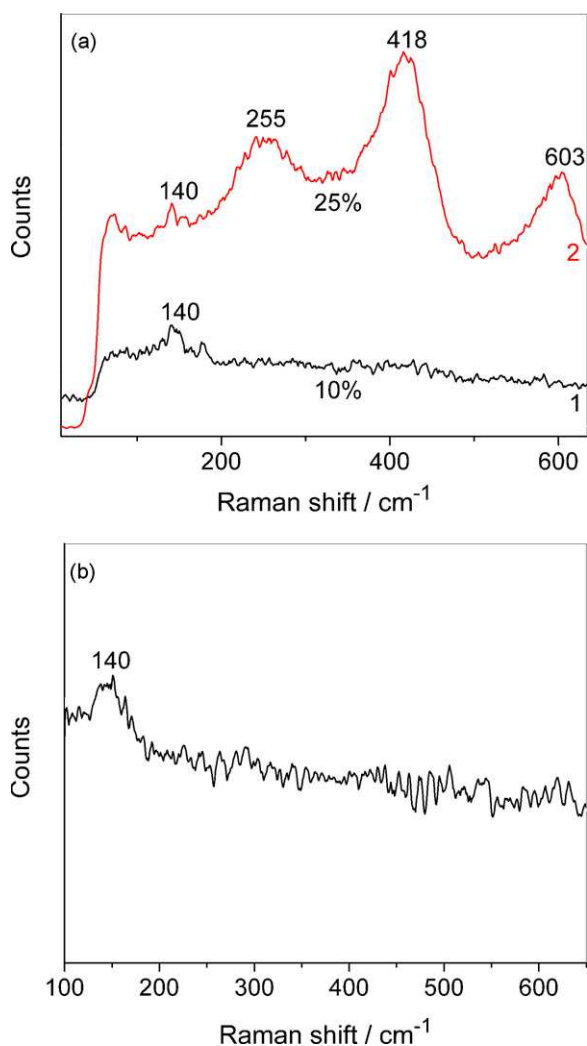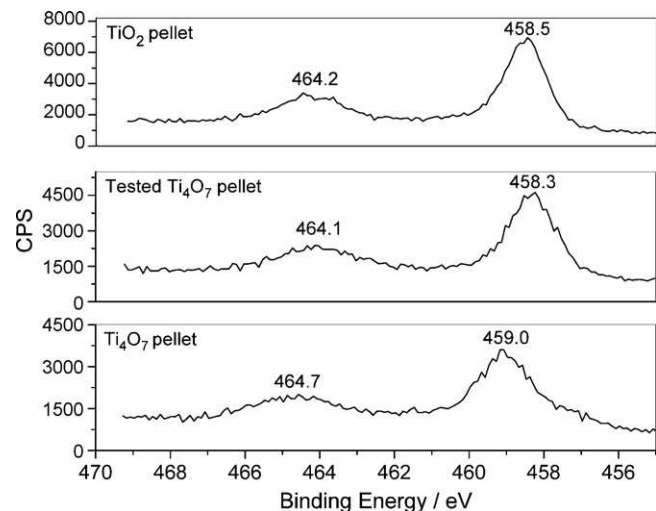
Fig. 11. XPS spectra for the surface of TiO_2 pellets (top), Ti_4O_7 pellet after stability testing at 0.55 V vs. Hg/HgO for 360 h (middle), and Ti_4O_7 pellet before testing (bottom).

Ti_4O_7 has its own characteristic BE values that are quite different from those of TiO_2. In the case of the Ti_4O_7 pellet, which was tested for 360 h at a potential of 0.55 V vs. Hg/HgO, the BE values tended to be identical to those of TiO_2 (Fig. 11), suggesting that a layer of TiO_2 was formed on the surface due to oxidation of Ti_4O_7 at high potential. In Fig. 10, the Raman spectra indicate that the Ti_4O_7 pellet could still present Ti_4O_7 features even after long-term testing. Considering that the probing depth of XPS is about 8 nm whereas that of Raman spectroscopy is about 1 μm, one may conclude that the TiO_2 layer formed on the Ti_4O_7 surface would be fairly thin and the oxidation of the Ti_4O_7 surface a fairly slow process. Unfortunately, we still cannot measure the exact thickness of the TiO_2 layer due to the limitations of our detecting instruments. The formation of a thin TiO_2 layer on the Ti_4O_7 surface might be beneficial in preventing the bulk of the Ti_4O_7 from being oxidized in concentrated alkaline solutions at high set potentials. Although a thin layer of TiO_2 might have formed on the Ti_4O_7 surface, the electrochemical activity of Ti_4O_7 did not seem to have been significantly affected.

4. Conclusions

In our exploration of new air-cathode materials for zinc-air rechargeable batteries, we successfully synthesized Ti_4O_7 using a TiO_2 reduction method. The obtained Ti_4O_7 material was characterized using XRD, Raman spectroscopy, and XPS. XRD results showed that the synthesized material was pure Ti_4O_7. This material was then coated on a glassy carbon electrode, and tested in concentrated KOH solutions for the ORR and the OER using cyclic voltammetry. The results indicated that this Ti_4O_7 material was active for the ORR and the OER. RRDE technique was used to obtain detailed electrode reaction kinetics for the ORR. Several parameters, such as overall electron transfer number, kinetic rate constants, electron transfer coefficients, and percentage H_2O_2 production were obtained based on the RRDE results and the Koutecky–Levich theory. The overall electron transfer number was found to be between 2.3 and 2.9 in 1, 4, and 6 M KOH electrolytes, suggesting that the ORR process on the Ti_4O_7 electrode was a mixed process between 2- and 4-electron transfer pathways. In order to test the feasibility of this Ti_4O_7 material in zinc-air rechargeable batteries, two kinds of electrochemical durability tests were carried out in a highly concentrated KOH electrolyte. The results showed Ti_4O_7 to be a stable material, suggesting that it should be a feasible candidate for air-cathodes in zinc-air batteries. To understand the stability of this material, Raman and

Fig. 10. Raman spectra for (a) original Ti_4O_7 pellet with tuning laser energy with (1) 10% filter irradiation (5×), (2) 25% filter irradiation; (b) Ti_4O_7 pellet after high-potential holding tests in O_2-saturated 6 M KOH electrolyte for 360 h, tuning laser energy filter set to 10%.

spond to the Raman-active modes of E_g, A_{1g}, and B_{2g}, respectively, for rutile TiO_2 [26]. This result suggests that oxidation of genuine Ti_4O_7 to rutile TiO_2 occurred on the surface, which was observable when the laser radiation was tuned to high excitation energy. The induced effect indicates that Raman spectroscopy is a useful technique for detecting Ti_4O_7, which has quite different features from those of rutile TiO_2. Fig. 10(b) displays the Raman spectra for Ti_4O_7 samples after 360 h of stability tests. Again, a feature peak at $140\,cm^{-1}$ can be observed, indicating that the bulk of the material was still Ti_4O_7.

To further study possible changes on the surface of this Ti_4O_7 material after long-term testing, XPS was used to study surfaces before and after testing. This is because the chemical composition of the Ti_4O_7 surface and their chemical states are responsible for achieving such a good stability. Fig. 11 shows the XPS spectra of the genuine Ti_4O_7 and the Ti_4O_7 pellet after the 360 h of holding-potential testing. For reference, Fig. 11 also presents the XPS spectrum for TiO_2. For a TiO_2 sample, Ti $2p_{3/2}$ and $2p_{1/2}$ photoelectron peaks can be found at binding energies (BE) of 458.5 and 464.2 eV, respectively. The BE of Ti $2p_{3/2}$ is consistent with that of pure rutile TiO_2 (458.55 eV) [27]. For the Ti_4O_7 sample before stability testing, the characteristic BE of Ti $2p_{3/2}$ in Ti_4O_7 can be observed at 459.0 eV, which is higher than in TiO_2. Hence, it is clear that the as-prepared

XPS spectra were collected from Ti_4O_7 samples before and after stability testing. The results and analysis revealed that a thin layer of TiO_2 formed on the Ti_4O_7 surface, which could prevent further oxidation from occurring in the bulk, stabilizing Ti_4O_7 electrode.

Acknowledgements

References

[1] H. Arai, S. Müller, O. Haas, J. Electrochem. Soc. 147 (2000) 3584.
[2] J. Goldstein, I. Brown, B. Koretz, J. Power Sources 80 (1999) 171.
[3] L. Swette, J. Giner, J. Power Sources 22 (1988) 399.
[4] G.Y. Chen, S.R. Bare, T.E. Mallouk, J. Electrochem. Soc. 149 (2002) A1092.
[5] N. Ross, H. Sokol, J. Electrochem. Soc. 131 (1984) 1742.
[6] L. Jörissen, J. Power Sources 155 (2006) 23.
[7] I. Roche, E. Chanînet, M. Chatenet, J. Vondrák, J. Appl. Electrochem. 38 (2008) 1195.
[8] E.E. Farndon, D. Pletcher, Electrochim. Acta 42 (1997) 1281.
[9] P.C.S. Hayfield, Development of a New Material-Monolithic Ti_4O_7 Ebonex Ceramic, Royal Society of Chemistry, Thomas Graham House.
[10] R.F. Bartholomew, D.R. Frankl, Phys. Rev. 187 (1969) 828.
[11] R.C. West (Ed.), CRC Handbook of Chemistry and Physics, CRC Press, 1987, p. F-122.
[12] C.B. Bezerra, L. Zhang, K.C. Lee, H.S. Liu, J.L. Zhang, Z. Shi, A.L.B. Marques, E.P. Marques, S.H. Wu, J.J. Zhang, Electrochim. Acta 53 (2008) 7703.
[13] U.A. Paulus, T.J. Schmidt, H.A. Gasteiger, R.J. Behm, J. Electroanal. Chem. 495 (2001) 134.
[14] A.J. Bard, L.R. Faulkner, Electrochemical Methods: Fundamentals and Applications, 2nd ed., John Wiley & Sons, New York, 2001.
[15] C.Z. Zhang, F.R.F. Fan, A.J. Bard, J. Am. Chem. Soc. 131 (2009) 177.
[16] K.E. Gubbins, R.D. Walker, J. Electrochem. Soc. 112 (1965) 469.
[17] D.R. Lide (Ed.), CRC Handbook of Chemistry and Physics, CRC Press, the content of the 90th Edition, 2009–2010.
[18] H. Meng, P.K. Shen, Electrochem. Commun. 8 (2006) 588.
[19] D.T. Sawyer, E.T. Seo, Inorg. Chem. 16 (1977) 499.
[20] T.J. Schmidt, H.A. Gasteiger, in: W. Vielstich, A. Lamm, H.A. Gasteiger (Eds.), Handbook of Fuel Cells, Fundamentals, Technology, and Applications, vol. 2 (Electrocatalysis), Wiley, 2003, Chapter 22.
[21] E. Yeager, J. Mol. Catal. 38 (1986) 5.
[22] R.W. Zurilla, R.K. Sen, E. Yeager, J. Electrochem. Soc. 125 (1978) 1103.
[23] A.J. Appleby, J. Marie, Electrochim. Acta 24 (1979) 195.
[24] M. Watanabe, Phys. Stat. Sol. (C) 6 (2009) 260.
[25] J.V. Landuyt, J. De Phys. 35 (1974) C7.
[26] V. Swamy, B.C. Muddle, Q. Dai, Appl. Phys. Lett. 89 (2006) 163118.
[27] G.Q. Li, C.Y. Liu, Y. Liu, Appl. Surf. Sci. 253 (2006) 2481.